# Chapter 16
# RayMan and SkyHelios Model

**Andreas Matzarakis, Marcel Gangwisch, and Dominik Fröhlich**

## 16.1 Introduction

Complex environments make it hard to assess meteorological parameters in a comprehensive and representative way (Matzarakis et al. 2010). One of the most complex environment types is the street level of urban areas (Hwang et al. 2011). The volume ranging from the ground to the roof level, the urban canopy layer (Oke 1987, p. 274), is the most relevant and at the same time most people are affected here. Measurements can only provide very limited insights, as the urban canopy layer is highly heterogeneous in time and space (Mirzaei and Haghighat 2010). Additionally, for most purposes spatial distributions of many meteorological and human-biometeorological parameters are required. Setting up lots of measuring stations and interpolating their readings to obtain spatial information for a desired area is mostly not an option due to being expensive and error-prone (Mirzaei and Haghighat 2010). Thus, for urban environments the application of urban microscale models is the most promising alternative (Hwang et al. 2011; Matzarakis et al. 2018), especially for the purpose of future planning and quantification of adaptation and mitigation measures (Herrmann and Matzarakis 2012; Ketterer and Matzarakis 2014).

This becomes even more complicated when thermal comfort or stress of humans is to be assessed. Information about thermal bioclimate is mostly generated by the calculation of thermal indices, e.g., predicted mean vote (PMV, Fanger 1972), physiologically equivalent temperature (PET, Höppe 1993, 1999; Matzarakis et al. 1999; Mayer and Höppe 1987), perceived temperature (PT, Staiger et al. 2012), universal thermal climate index (UTCI, Jendritzky et al. 2012), standard effective

A. Matzarakis (✉) · M. Gangwisch · D. Fröhlich
Research Centre Human Biometeorology, German Meteorological Service,
Freiburg, Germany
e-mail: andreas.matzarakis@dwd.de; marcel.gangwisch@dwd.de; dominik.froehlich@mailbox.org



M. Palme, A. Salvati (eds.), *Urban Microclimate Modelling for Comfort and Energy Studies*, https://doi.org/10.1007/978-3-030-65421-4_16

temperature (SET*, American Society of Heating 2005; Gagge et al. 1986; Gonzalez et al. 1974), or modified physiologically equivalent temperature (mPET, Chen and Matzarakis 2018). These thermal indices combine meteorological and thermo-physiological aspects to approximate the thermal perception of a sample human being (Höppe 1993). Most thermal indices do allow for the setting of the physiological parameters: age, weight, height, metabolic rate and activity, as well as posture and sex (e.g., PMV, PET, mPET, and PT). The meteorological variables for all the indices mentioned above are air temperature ($T_a$), vapor pressure (VP), wind speed ($v$), and different radiation fluxes (e.g., Fanger 1972; Höppe 1999; Jendritzky et al. 2012; Staiger et al. 2012). The short- and long-wave radiation fluxes from and to the sample person are usually summarized as the mean radiant temperature ($T_{mrt}$). $T_{mrt}$ is defined as the surface temperature of a perfect black and equal surrounding environment, which leads to the same energy balance as the current environment (Fanger 1972; VDI 1988, 2008).

## 16.2 Methods and Data

### *16.2.1 Thermal Indices*

Human beings have no senses to "feel" individual meteorological parameters. In particular, humans are unable to distinguish between heat stress by actinic and thermal processes (e.g., radiation and air temperature). They rather feel the integral effect of several parameters in terms of modification to their skin as well as to their blood temperature (Staiger et al. 2018, 2019). The thermal sensation of humans, as well as the physiological strain, can be assessed by thermal indices.

#### 16.2.1.1 Perceived Temperature

The perceived temperature (PT) is an equivalent temperature for the assessment of human thermal comfort based on the human energy balance model "Klima-Michel model" (Staiger et al. 2012), which is designed for outdoor use. Thermal assessment in PT is based on a modification of the (indoor) thermal index predicted mean vote (PMV, Fanger 1972) after Gagge et al. (1986). PT is defined as "the air temperature of a reference environment in which the thermal perception would be the same as in the actual environment" (Staiger et al. 2012, 2019). The perceived temperature does consider a self-adapting clothing model that will automatically try to achieve thermally comfortable conditions. In case it fails to do so, thermal stress is occurring.

#### 16.2.1.2 Universal Thermal Climate Index

The universal thermal climate index (UTCI), like PT, is an equivalent temperature. In UTCI the meteorological conditions are compared to a reference environment with 50% relative humidity, calm air, and $T_{mrt}$ being equal to $T_a$ (Jendritzky et al. 2012). UTCI is defined as "the isothermal air temperature of the reference condition that would elicit the same dynamic response (strain) of the physiological model" (Jendritzky et al. 2012). UTCI calculates the current heat load based on a heat transfer model (Fiala et al. 2012) considering a fully automatic clothing model (Havenith et al. 2012) adapting to the current meteorological conditions. For being too complex to be determined numerically, UTCI is usually estimated based on a regression equation (Bröde et al. 2012). While the regression speeds up the calculation, it limits the possible input to the meteorological parameters: air temperature, vapor pressure, wind speed (at a height of 10 m), as well as mean radiant temperature. In addition, the range of parameters is restricted by the regression. For example, $T_a$ may only vary from −50 to +50 °C, and wind speed may range from 0.5 to 17.0 m/s. If the conditions are exceeding the limits, there are workarounds proposed allowing to calculate UTCI anyway, but with some imprecision (Bröde et al. 2012).

#### 16.2.1.3 Physiologically Equivalent Temperature

A widely applied thermal index for all kinds of studies about human thermal comfort is the physiologically equivalent temperature (PET, Höppe 1999; Mayer and Höppe 1987). It is defined as "the air temperature at which, in a typical indoor setting (without wind and solar radiation), the energy budget of the human body is balanced with the same core and skin temperature as under the complex outdoor conditions to be assessed" (Höppe 1999). PET is based on a simplified version of the human energy balance model "Munich energy balance model for individuals" (MEMI, Höppe 1984). In contrast to PT and UTCI, the clothing model in PET is not self-adapting. This allows for the setting of a clothing insulation in terms of the clothing index clo.

#### 16.2.1.4 Standard Effective Temperature

The standard effective temperature (SET*, American Society of Heating 2005; Gagge et al. 1986; Gonzalez et al. 1974) is originally defined as the equivalent dry bulb temperature of an isothermal environment. The environment is at 50% relative humidity and 0.25–0.3 m/s wind speed in which a human being would have the same heat stress (skin temperature) and thermoregulatory strain (skin wetness) as in the actual environment.

#### 16.2.1.5 Modified Physiologically Equivalent Temperature

The modified physiologically equivalent temperature (mPET, Chen and Matzarakis 2018) is a further development of PET adding a self-adapting or manual clothing model, as well as an improved consideration of humidity.

### *16.2.2 Human Biometeorological Models*

#### 16.2.2.1 RayMan

The RayMan model is a microscale model developed at the Chair for Environmental Meteorology of the University of Freiburg, calculating radiation fluxes in simple and complex urban environments (Matzarakis et al. 2007, 2010). This allows for the estimation of $T_{mrt}$, which is an important input parameter for the calculation of thermal indices like PT, UTCI, and PET.

RayMan is one-dimensional in space (all calculations are performed for a single point in space). It is a diagnostic model and therefore fully time independent. RayMan was developed with performance and usability in mind. All calculations and settings can be set up and controlled through the graphical user interface (Fig. 16.1). The short runtime is a precondition to run calculations for long datasets covering several years in high temporal resolution (e.g., Fröhlich and Matzarakis 2013).

Another idea behind RayMan is to require only a minimal number of meteorological parameters as input and all of them being parameters that are typically recorded at normal climate stations (Matzarakis et al. 2010). Due to the one-dimensionality of the model, the output of the model is only valid for the given meteorological input conditions. For a spatial output and spatially varying conditions consider the SkyHelios model.

A key feature of RayMan is the calculation of the sky view factor (SVF, the fraction of free sky within the upper hemisphere) from either a fisheye image or a spatial input in terms of an obstacle file. RayMan obstacle files include the surrounding urban morphology of the point of interest. The local, spherical SVF can be used to estimate the mean radiant temperature for the current location.

The obstacle file's format is defined as a vector-based ASCII file format, which can be created manually using the RayMan obstacle editor or exported from other spatial geodata using the plug-in "Shp to Obs" developed for Quantum GIS (QGIS, Open Source Geospatial Foundation 2018).

RayMan is capable of considering resolved objects of the urban environment (buildings and trees). These are saved in obstacle files (obs) in a specific format. Obstacle files are raw plain text files containing a header and each individual obstacle:

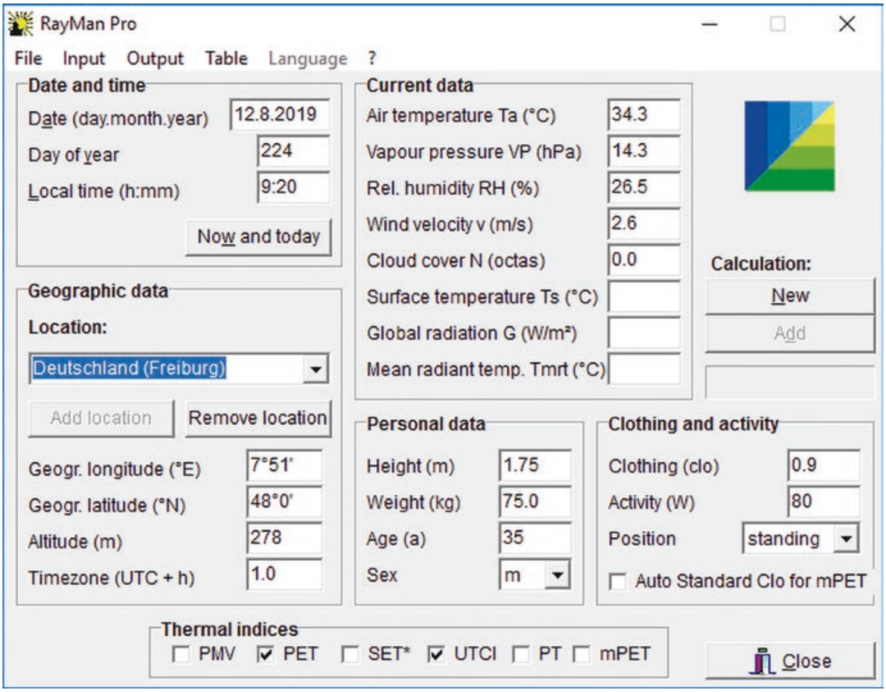


**Fig. 16.1** RayMan main window, showing the graphical user interface of RayMan. All meteorological variables required to estimate thermal sensation by thermal indices

```
# RayMan Pro obstacle file #
# Building with roof and bottom coordinates
g     6.25 17.38 10.00 6.75 7.75 10.00 15.13 7.13 10.00
      14.75 17.25 10.00 6.25 17.38 0.00 6.75 7.75 0.00
      15.13 7.13 0.00 14.75 17.25 0.00
      0.30 0.95     # albedo and emissivity

# Broadleaf tree with x, y coordinate, tree height,
# crown radius, trunk height, trunk diameter,
# albedo and emissivity
l     3.88 12.38 10.00 3.33 4.00 0.33 0.30 0.95

# Coniferous tree
n     12.88 1.75 10.00 5.00 4.00 0.00 0.25 0.96
```

The obstacle files can be displayed and modified using a plain raw text editor (e.g., Vim, Notepad++). Thereby one obstacle is defined in one individual row. A building obstacle is represented in one line by the *g* keyword. The coordinates of the building are given in a subsequent way, defining all corners of the building, by specifying the roof and the bottom corners of the building (*x*, *y*, *z* coordinate in red, blue, green). The line of an obs file in RayMan Pro ends with the albedo and the emissivity of the obstacle. Trees are defined by a different keyword: *l* for deciduous tree and *n* for coniferous trees. The keyword is followed by *x*- and *y*-positions, tree height, crown radius, trunk height, trunk diameter, albedo, and emissivity.

#### 16.2.2.2 SkyHelios

SkyHelios is a model for the rapid estimation of spatially resolved atmospheric parameters like sky view factor (SVF, Matzarakis and Matuschek 2011), sunshine duration, global radiation ($G$), wind speed ($v$) and wind direction (WD), mean radiant temperature ($T_{mrt}$), as well as thermal indices in a complex urban environment (Fröhlich and Matzarakis 2018).

It applies the managed Object-Oriented Graphics Rendering Engine (MOGRE), initially developed for video games, to create a virtual three-dimensional environment (Fig. 16.2) from any spatial input data (Ogre Development Team 2019). The idea behind this approach is faster calculations using rather affordable hardware (Matzarakis and Matuschek 2011). Another advantage of utilizing the graphics engine is the fast and simple determination of reflections in the radiation calculations by making use of the scene lighting and shading capabilities (Fröhlich and Matzarakis 2018).

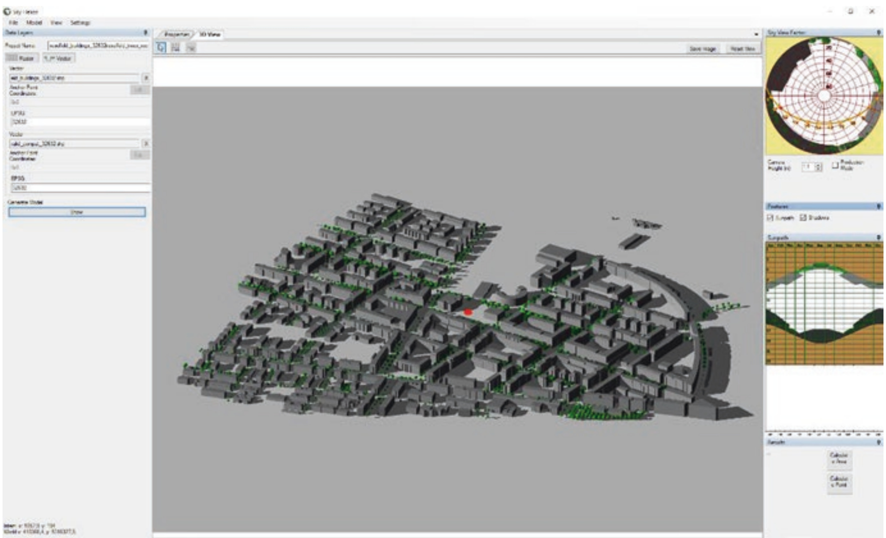

**Fig. 16.2** SkyHelios main window, showing the 3D study area with buildings (gray) and urban trees (green). The red dot specifies a point of interest and determines the calculation of sky view factor for single points (top, right). The diagram (center, right) gives an overview of the sun path throughout the day and year

Like RayMan, SkyHelios is a fully diagnostic model (Fröhlich and Matzarakis 2018). Therefore, the steady-state model is time independent allowing for running the model for specific points in time without having to consider any spin-up period. The model, e.g., can calculate for 20.03.2019 14:00 UTC, 23.09.2019 14:00 UTC, and 22.12.2019 14:00 UTC the proposed parameters. Meteorological input data for each time step (date and time) desired can be provided by a delimited text file (Fröhlich and Matzarakis 2018).

Another big advantage of the SkyHelios model is the various spatial input options. The SkyHelios model accepts a wide range of well-known spatial formats. These are to be divided into raster and vector formats. Raster formats consist of equidistant grids of parameters (e.g., elevation) for every grid cell. SkyHelios is capable of importing the most common raster file formats by including the Geospatial Data Abstraction Library (GDAL, GDAL/OGR Contributors 2019). Vector formats, on the contrary, do specify the position of corners and points in the outline of obstacles (vertices). Several vertices together can form polygons representing, e.g., buildings. It is necessary that input files incorporate three-dimensional data either by providing an additional height field or by polygons based on three-dimensional vertices. A very common example for vector file formats is the ESRI shapefile format. SkyHelios can read a number of vector formats by including the OpenGIS Simple Features Reference Implementation library (OGR, GDAL/OGR Contributors 2019). RayMan obstacle files can be imported as well. Starting from the passed urban geometry data, a three-dimensional model of the city is rendered by the MOGRE engine.

Based on the provided input, several astronomical, meteorological, as well as biometeorological quantities can be estimated both spatially (area of interest) and for individual preselected points in space (point of interest). The parameter sky view factor (planar and spherical, Hämmerle et al. 2011) can be estimated from rendered fisheye imagery within the provided model domain. SVF can be further utilized to derive the radiation properties in the urban radiational regime (short- and long-wave radiation fluxes from the upper and lower hemisphere).

The mean radiant temperature ($T_{\mathrm{mrt}}$) summarizes all radiation fluxes and is the most important parameter for human thermal comfort assessment. $T_{\mathrm{mrt}}$ is dependent on astronomic conditions (e.g., solar altitude and azimuth angle), atmospheric conditions (e.g., relative humidity, cloud cover, air temperature, surface temperature of the neighborhood, global radiation (divided into direct and diffuse radiation)), and surrounding urban morphology (with different albedo and emissivity coefficients).

$T_{\mathrm{mrt}}$ can be determined by solving the Stefan-Boltzmann law for all surrounding surfaces $i$ of the neighborhood (Matzarakis et al. 2007):

$$T_{\mathrm{mrt}} = \sqrt[4]{\sum_i \left( \epsilon_{\mathrm{lw},i} \cdot T_{\mathrm{s},i}^4 + \frac{\alpha_{\mathrm{abs,s},i} \cdot D_{\mathrm{s},i}}{\epsilon_{\mathrm{lw,p}} \cdot \sigma} \right) \cdot \mathrm{Pr}_{\mathrm{p},i}} \left[ ^{\circ}\mathrm{C} \right] \quad (16.1)$$

$T_{mrt}$ is dependent on the surface's long-wave emissivity ($\epsilon_{lw,\,i}$), surface's temperature ($T_{s,i}$), surface's short-wave absorption coefficient (1.0 – albedo, $\alpha_{abs,\,s,\,i}$), surface's absorbed scattered reflected global radiation ($D_{s,i}$), surface's projection factor ($Pr_{p,i}$), and Stefan-Boltzmann constant $\left(\sigma = 5.67 \times 10^{-8}\,\mathrm{W} \cdot \mathrm{m}^{-2} \cdot T_s^{-4}\right)$. An emissivity of 0.97 is applied to the human body (Fanger 1972).

The calculation pipeline for the mean radiant temperature in SkyHelios is depicted in Figs. 16.3, 16.4, and 16.5:

$T_{mrt}$ in SkyHelios is calculated based on the radiational impact of the lower and upper hemispheres for long- and short-wave radiation fluxes. Direct and scattered short-wave radiation fluxes (including single reflections by the neighborhood) as well as long-wave emittance of the ground and the surroundings are considered (Fig. 16.3). In order to obtain better approximations for radiation fluxes, short- and long-wave radiation fluxes are considered separately:

The calculation of direct short-wave radiation flux ($I$) is assumed to be independent of SVF for unshaded locations and zero for shaded conditions (Fig. 16.4). According to Jendritzky (1990), $I$ can be estimated as a function of the solar constant ($I_0$), solar zenith angle based on Bouguer-Lambert's equation in combination with the relative optical air mass ($r_{opt}$), optical depth of the atmosphere ($\delta_{opt}$), and Linke turbidity factor ($T_L$):

$$I = I_0 \cdot \exp\left(-\delta_{opt} \cdot T_L \cdot r_{opt} \cdot \frac{p}{p_0}\right) \cdot \cos(\zeta) \cdot \left(1 - \frac{cc}{8}\right) \tag{16.2}$$

The relative optical air mass can be estimated after (Kasten and Young 1989) as a function of solar azimuth angle ($\zeta$):

$$r_{opt} = \left(\sin\left(90^\circ - \zeta\right) + 0.50572 \cdot \left(\left(90^\circ - \zeta\right) + 6.07995^\circ\right)^{-1.6364}\right)^{-1} \tag{16.3}$$

The optical depth is described by the optical air mass (Kasten 1980):

$$\delta_{opt} = \frac{1}{0.6 \cdot r_{opt} + 9.4} \tag{16.4}$$

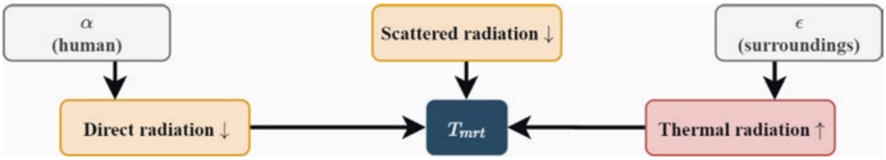


**Fig. 16.3** Composition of the long- and short-wave radiation fluxes (red and orange, respectively) for the calculation of the mean radiant temperature ($T_{mrt}$) for given surface properties (albedo ($\alpha$) and emissivity ($\epsilon$))

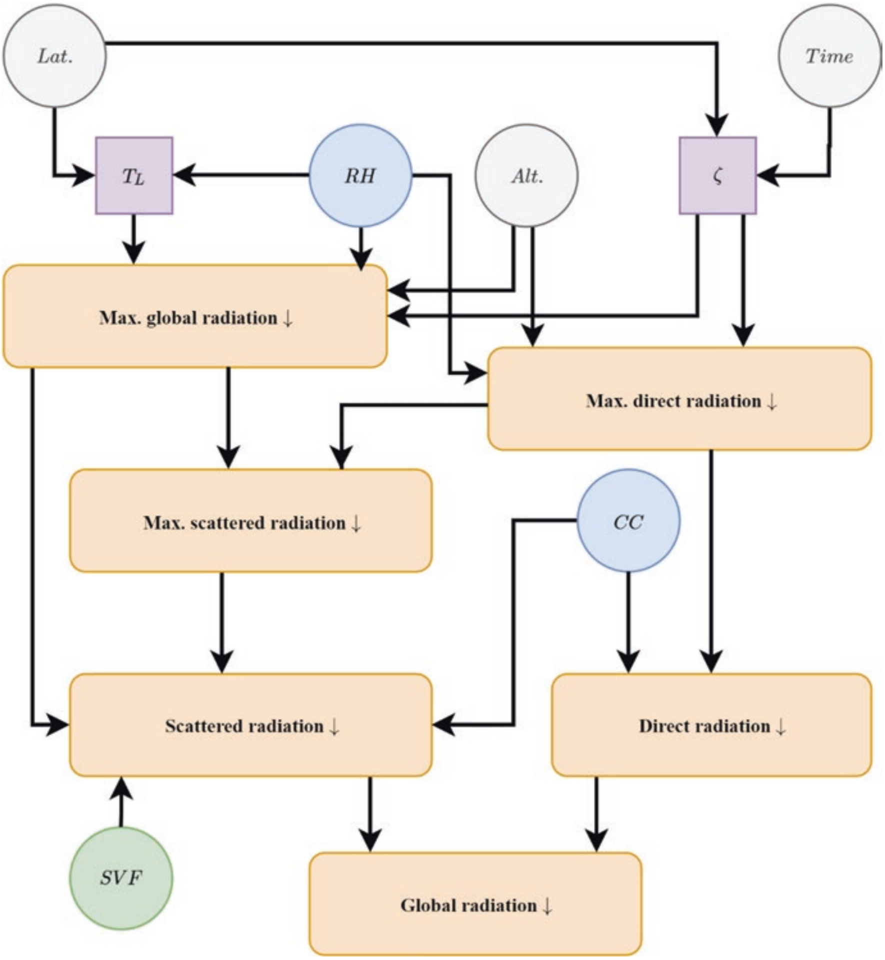


**Fig. 16.4** Calculation of short-wave radiation fluxes for diffuse (based on SVF) and direct solar radiation (based on the visibility of the sun) for given cloud cover (CC) and relative humidity (RH), depending on the geographical parameters for location (latitude (lat) and altitude (alt)) and time

The diffuse short-wave irradiation is calculated from the direct solar irradiation as the sum of isotropic and anisotropic scattered radiation ($D = D_{iso} + D_{aniso}$) (Valko 1966). The isotropic part is calculated by the following equation:

$$D_{iso} = \left(G_0 - I_{clear}\right) \cdot \left(1 - \frac{I_{clear}}{I_0 \cdot \cos(\zeta)}\right) \cdot \mathrm{SVF} \tag{16.5}$$

The direct solar irradiation for clear sky conditions (without clouds and horizon limitations) is calculated based on Eq. (16.2) (for CC = 0). The anisotropic fracture of the scattered radiation can be approximated if the sun is visible (Valko 1966):

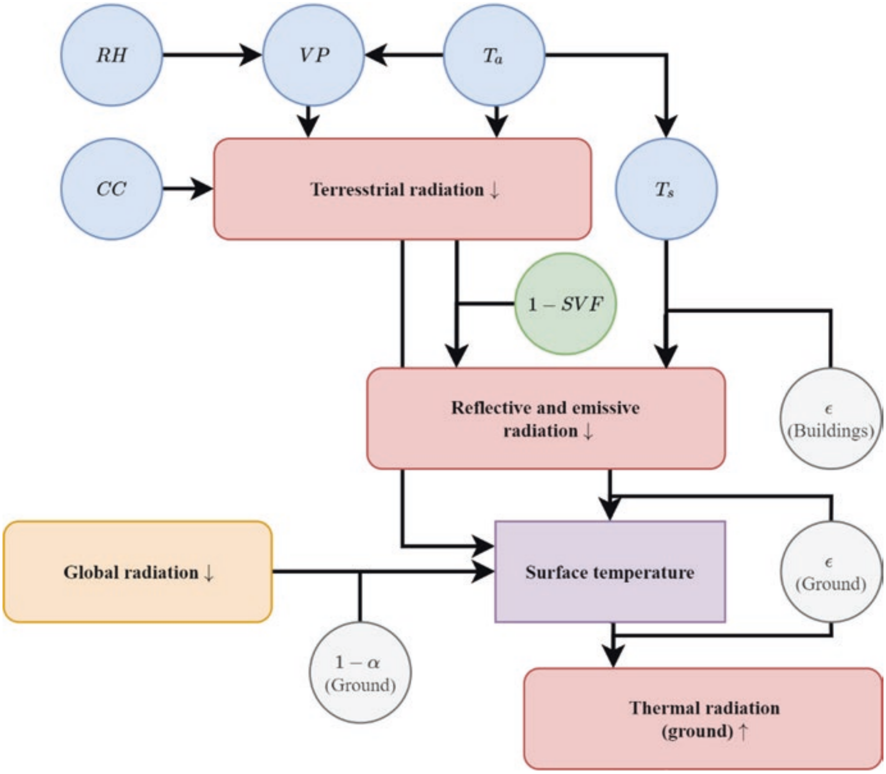


**Fig. 16.5** Estimation of the long-wave radiation (red) emitted from the lower hemisphere for the $T_{\text{mrt}}$ calculus. Terrestrial radiation from the atmosphere (based on meteorological conditions (blue)) and reflected and emitted long-wave radiation from the neighborhood (based on surface properties (gray)) are considered

$$D_{\text{aniso}} = \left(G_0 - I_{\text{clear}}\right) \cdot \frac{I_{\text{clear}}}{I_0 \cdot \cos(\zeta)} \tag{16.6}$$

The global radiation ($G_0$) for clear sky conditions can be directly calculated as proposed by Jendritzky (1990) and VDI (1994, 2008) for given air pressure (pr), $T_L$ and $\zeta$:

$$G_0 = 0.84 \cdot I_0 \cdot \cos(\zeta) \cdot \exp\left(\frac{-0.027 \cdot \frac{\text{pr}}{\text{pr}_0} \cdot T_L}{\cos(\zeta)}\right) \tag{16.7}$$

These fluxes are calculated based on given short-wave albedo and long-wave emission coefficients for each urban obstacle in the neighborhood. The estimation of the long-wave radiation fluxes as depicted in Fig. 16.5 is mainly based on the Stefan-Boltzmann law for a gray body (e.g., non-perfectly black surface) (Fanger 1972; VDI 2008):

$$P_{lw} = \epsilon \cdot \sigma \cdot A_s \cdot T_s^4 \tag{16.8}$$

Based on this law, SkyHelios calculates the surface temperature ($T_s$) and emitted long-wave radiation flux density ($P_{lw}$), and vice versa. The emitted long-wave radiation depends on $\epsilon$ of the surface as well as on $\sigma$.

Besides the calculation of $T_{mrt}$, SkyHelios is capable of sunshine duration, wind speed and direction (Fröhlich 2017; Fröhlich et al. 2019; Fröhlich and Matzarakis 2018), and aerodynamic roughness (Ketterer et al. 2017). Based on these, the thermal indices PT, UTCI, and PET can be calculated for any location within the model domain.

### *16.2.3 Area of Interest*

A study area in the West of Freiburg (South-West Germany), the urban quarter *Rieselfeld* is selected for this study. The district has an extent of 1015 m on 916 m (0.92 km$^2$) and is located at 47.9991 N, 7.7921 E, 232 m a.s.l. The whole area can be divided into 0.15 km$^2$ built-up area and 0.77 km$^2$ free space. Detailed spatial input of the buildings in terms of a level of detail (LOD) 1, as well as a LOD 2 city model (based on the CityGML data format (Gröger et al. 2012)) and an urban tree cadaster, was provided by the municipality of Freiburg. The model is applied for the specified spatial resolution of 1 m, resulting in a discrete model domain of 1054 on 916 grid cells. All results are assessed for the target height of 1 m.

### *16.2.4 Meteorological Input Data*

As a sample dataset, records of the official weather station 01443 (Freiburg airport) of the German Meteorological Service were selected, providing the data via the Climate Data Center (CDC). The meteorological input comprises the parameters air temperature (°C), relative humidity (%), air pressure (hPa), wind speed (m/s) and direction (°), as well as global radiation (W/m$^2$) for the whole day in 10-min temporal resolution.

From the dataset, July 25, 2019, was selected for the analysis in this study. The day is selected for being part of a heat wave and for providing clear-sky conditions. The maximum of the solar altitude angle is 64.6° (11:36 UTC), while solar azimuth angle ranges from 58.5° during sunrise (05:55 UTC) to 301.0° during sunset (21:14 UTC).

The prevailing air temperature rises from 17.5 °C in the morning (04:20 UTC) to 37.2 °C in the afternoon (15:00 UTC). Together with the low wind speed of 0.0–4.7 m/s in 10 m height and the global radiation of up to 855 W/m$^2$, thermal stress is to be expected.

## 16.3 Results and Discussion

Human thermal sensation is assessed for the prevailing weather conditions of July 25, 2019. Besides the final output, intermediate results, which are required to quantify human thermal comfort in terms of thermal indices, are analyzed. The spatial resolution for all calculations is 1 m per default, but may be specified on demand in SkyHelios.

### *16.3.1 Intermediate Results*

#### 16.3.1.1 Obstruction of the Upper Hemisphere: Analysis by the Spherical Sky View Factor

The obstruction of the upper hemisphere by the urban morphology (e.g., buildings and trees), in terms of the spherical and planar sky view factor (SVF) (Hämmerle et al. 2011), can be calculated by SkyHelios (Fig. 16.6). SVF is the fraction of the visible sky, as seen from a certain point (Oke 1987, p. 353). Spherical SVF is shown here, because it is more suitable for issues about objects with a vertical extension (e.g., human body), which can be represented by a cylinder, instead of a plane. Planar SVF can be applied for flat surfaces (e.g., the calculation of material heating and reflection) (Hämmerle et al. 2011). The urban environment is built up by vertical surfaces. Urban areas with wide spaces and small obstacles are represented by high SVF, whereas areas with narrow street canyons and high obstacles are more obstructed, resulting in a low SVF.

The spatial mean of spherical SVF for the study area is 0.67, while SVF ranges from 0.99 at the borders to 0.05 in the center of the study area beside buildings. Planar SVF is in the range of 0.07–0.99 with an average of 0.78. SVF is calculated in 1 m spatial resolution, so that 965,464 values for the land area of 0.93 km$^2$ are calculated.

The spatial average of SVF can be compared to SVF footprints of other cities (Middel et al. 2018) in order to characterize the city in terms of superelevation of the horizon. According to Middel et al. (2018, 2019), SVF can be assessed from Google Street View Imagery, based on four cardinal images and one image facing upwards. The study area in Freiburg (average planar SVF: 0.78, spherical SVF: 0.67) is comparable to Bonn (average planar SVF: 0.74). Nevertheless, SVF by Google Street View is only available for specific points along streets. “Google Street View


**Fig. 16.6** The obstruction of the upper hemisphere by the urban morphology (e.g., buildings and trees) can be calculated by SkyHelios in terms of spherical and planar sky view factor (SVF). SVF can be computed spatially resolved with variable resolution for different urban environments due to preexisting urban city models. This SVF is calculated for 12:00 UTC on July 25, 2019, in 1 m height

images are inherently biased towards street locations and therefore do not provide continuous spatial coverage of the urban environment" (Middel et al. 2018). For the land area of 141.1 km$^2$ only 93,188 locations have been used for the estimation of SVF in Bonn. This leads to a spatial density of 0.0006 SVF estimation per m$^2$. Therefore, the spatial resolution and the density of SkyHelios (in this case 1 m) cannot be reached. This leads to the assumption that the spatial density of Google Street View imagery is not sufficient in order to assess spatially resolved SVF. The estimation of SVF by Google Street View imagery is also limited to the fixed target height of 2 m, while the user of SkyHelios can determine the target height freely.

#### 16.3.1.2 Limited Direct and Diffuse Short-Wave Radiation by Shading: Analysis by the Mean Radiant Temperature

The sky view factor (SVF) has a direct impact on the incoming short- and long-wave radiation fluxes within the urban radiation regime. The effects of all different short- and long-wave radiation fluxes in the study area are shown in Fig. 16.7 as $T_{mrt}$. Shading of direct and diffuse short-wave radiation by urban geometries (e.g., buildings) as well as urban vegetation is clearly observable in $T_{mrt}$ (blue areas with reduced $T_{mrt}$). SkyHelios is able to model full shading as well as partial shading. Therefore, it is possible to distinguish between shading by buildings and shading by vegetation. The mean $T_{mrt}$ in shaded areas by buildings is 48.9 °C (ranging from 45.2 to 54.6 °C) compared to the mean $T_{mrt}$ in shaded areas by vegetation 49.9 °C (ranging


**Fig. 16.7** The effect of all different short- and long-wave radiation fluxes in the urban environment can be calculated by SkyHelios in terms of the mean radiant temperature ($T_{mrt}$). $T_{mrt}$ is calculated for 12:00 UTC on July 25, 2019

from 46.6 to 53.6 °C). The mean $T_{mrt}$ in sunlit areas is 62.2 °C (ranging from 57.7 to 73.7 °C). Therefore, shade by buildings reduces $T_{mrt}$ by 13.3 °C, while shade by vegetation reduces $T_{mrt}$ by 12.3 °C compared to sunlit areas.

Different types of shade can explain this difference. While buildings block solar irradiance completely, vegetation can be considered as porous media, allowing for partial transmission of solar radiation. For the study area this makes a difference of 1 °C in terms of $T_{mrt}$. The effect of porosity has to be further discussed under the aspect of wind speed and direction. The size of the shaded area of buildings and vegetation is dependent on solar altitude and solar azimuth angle and therefore on time of the day, day of the year, and geographical latitude.

The shaded area by buildings in the study area is 0.08 km$^2$ (10.38% of the area with free space), while 0.03 km$^2$ (3.9% of the area with free space) of shade is provided by vegetation.

#### 16.3.1.3 Diagnostic Wind Speed and Direction

SkyHelios is capable of running a diagnostic steady-state wind model to simulate a time-independent wind field (Fröhlich et al. 2019). Modelled wind speed and direction are further incorporated into the assessment of human thermal comfort, to consider the effect of wind chill. The sensitivity of thermal indices with high wind speed has been described by Fröhlich and Matzarakis (2016). The incident wind (3 m/s from 350°) is modified by the urban morphology, resulting in wind speeds between 0.0 and 6.2 m/s. The magnitude of the mean wind speed is 1.2 m/s.

Sheltering effects near buildings, which are orthogonal to the prevailing wind direction, are observable with reduced wind speed. Wind speed is significantly increased in narrow-street canyons, which are aligned to incident wind, due to channeling effect (Fig. 16.8).

### *16.3.2 Spatial Assessment of the Outdoor Thermal Sensation*

Thermal sensation and physiological strain due to heat load and radiation interception are quantified in terms of the physiologically equivalent temperature (PET). PET varies between 40.4 and 61.2 °C. The mean PET is 47.5 °C approving the assumption of heat stress for July 25, 2019, in Rieselfeld, Germany. According to the scale for thermal perception (Matzarakis and Mayer 1996), physical strain is equivalent to e*xtreme heat stress* (Table 16.1). Impact of decreased wind speed (sheltering effect) at the lee side of buildings, increased wind speed (channeling effect) in narrow-street canyons, as well as shading by buildings and vegetation is clearly visible (Fig. 16.9). Spatial mean of PET in shaded areas by urban obstacles (e.g., shading by buildings) is 42.9 °C (ranging from 40.37 to 46.1 °C), compared to the spatial mean of PET in shaded areas by vegetation 42.8 °C (ranging from 41.1 to 46.4 °C). PET in sunlit areas varies between 45.5 and 61.2 °C with an average of 48.4 °C. Therefore, building's shade reduces mean thermal strain on average by 5.5 °C, while vegetation's shade reduces heat stress on average by 5.6 °C in terms of PET. The air temperature and humidity in the model are assumed to be constant


**Fig. 16.8** Diagnostic wind speed under prevailing boundary conditions of 3 m/s and a wind direction of 350°, calculated by SkyHelios. Wind speed and wind direction are calculated for 12:00 UTC on July 25, 2019

**Table 16.1** Thermal sensation classes for human beings in Central Europe (based on an internal heat production of 80 W and a heat transfer resistance of the clothing of 0.9 Clo) by Matzarakis and Mayer (1996)

| PET (°C) | Thermal perception | Level of physiological stress |
|---|---|---|
| ≥41 | Very hot | Extreme heat stress |
| 35–41 | Hot | Strong heat stress |
| 29–35 | Warm | Moderate heat stress |
| 23–29 | Slightly warm | Slight heat stress |
| 18–23 | Comfortable | No thermal stress |
| 13–18 | Slightly cool | Slight cold stress |
| 8–13 | Cool | Moderate cold stress |
| 4–8 | Cold | Strong cold stress |
| <4 | Very cold | Extreme cold stress |


**Fig. 16.9** SkyHelios can assess human thermal comfort in terms of the physiologically equivalent temperature (PET). PET can be computed spatially resolved with variable spatial resolution for different urban environments by SkyHelios. PET is calculated for 12:00 UTC on July 25, 2019

throughout the study area. The temperature of different surfaces in the model domain is not coupled with the air temperature by now. In addition to that, cooling by biophysiological processes (e.g., transpiration and photosynthesis) is also not included in the model, but can reduce air temperature in green parks by 0.94 °C according to literature (Bowler et al. 2010) or even up to 2.0 °C (Zardo et al. 2017). This would also reduce thermal heat stress.

### 16.3.3 Temporal Analysis of the Thermal Sensation

SkyHelios can also be used to run simulations for long time series. The calculation is conducted locally for one point of interest, instead of the complete study area. The time series is calculated in accordance to the predefined meteo input file (10-min temporal resolution). It is possible to select all named human biometeorological parameters.

The diurnal cycle of the thermal indices physiologically equivalent temperature (PET) and Universal Thermal Climate Index (UTCI), recorded wind speed, modelled wind speed, mean radiant temperature, and global radiation throughout the day (July 25, 2019) for a predefined location of interest (easting: 409863, northing: 5316954—EPSG:32632) are presented in Fig. 16.10. Both indices show the same diurnal cycle but vary in magnitude. UTCI is systematically of higher magnitude compared to PET during night, while PET results in higher values during the day. In both cases, thermal heat load is reduced with increasing wind velocity and decreasing mean radiant temperature.

PET varies between 30.9 and 49.8 °C with an average of 38.7 °C, while UTCI is in the range of 34.2–43.2 °C with an average of 37.4 °C.

Thermal heat stress is reduced with increasing wind speed in the afternoon. The modelled diagnostic wind speed is of same shape compared to recorded wind velocity at the station, but is systematically reduced by increased aerodynamic roughness of the built-up urban neighborhood in the proximity to the point of interest. The modelled wind velocity varies between 0.0 and 2.7 m/s, while the recorded dataset ranges from 0.0 to 4.7 m/s. Mean wind speed is reduced due to the neighborhood by 0.8 m/s.

Mean radiant temperature follows a similar diurnal cycle compared to global radiation but is damped during midday and in the late afternoon. The mean radiant temperature curve corresponds to a Gaussian bell curve, with a minimum of 26.4 °C, maximum of 62.7 °C, and an average value of 40.3 °C.

$T_{mrt}$ is dependent on the local, spherical sky view factor (SVF). Spherical SVF for the location of interest is 0.77 (planar SVF: 0.94). The corresponding fisheye image is shown in Fig. 16.11. It also shows the sun path at the selected day and location.

Thermal sensation is assessed by UTCI and PET, while thermal perception differs between these indices. PET evaluates the prevailing meteorological conditions from *warm* in the night (from 00:00 to 07:00 UTC and from 17:00 to 23:50 UTC) to *very hot* (during noon at 11:20 UTC), associated with *strong* to *extreme heat stress*. The range of UTCI values is denser, resulting in lower level of physiological stress. The conditions assessed by UTCI vary between *warm* and *hot*, associated with mainly *strong* and *very strong heat stress* according to the UTCI classification of thermal stress (Table 16.2) (Błażejczyk et al. 2013).

UTCI classification is a classification for heat stress while PET classes are suitable for the assessment of thermal comfort and discomfort. Both indices are

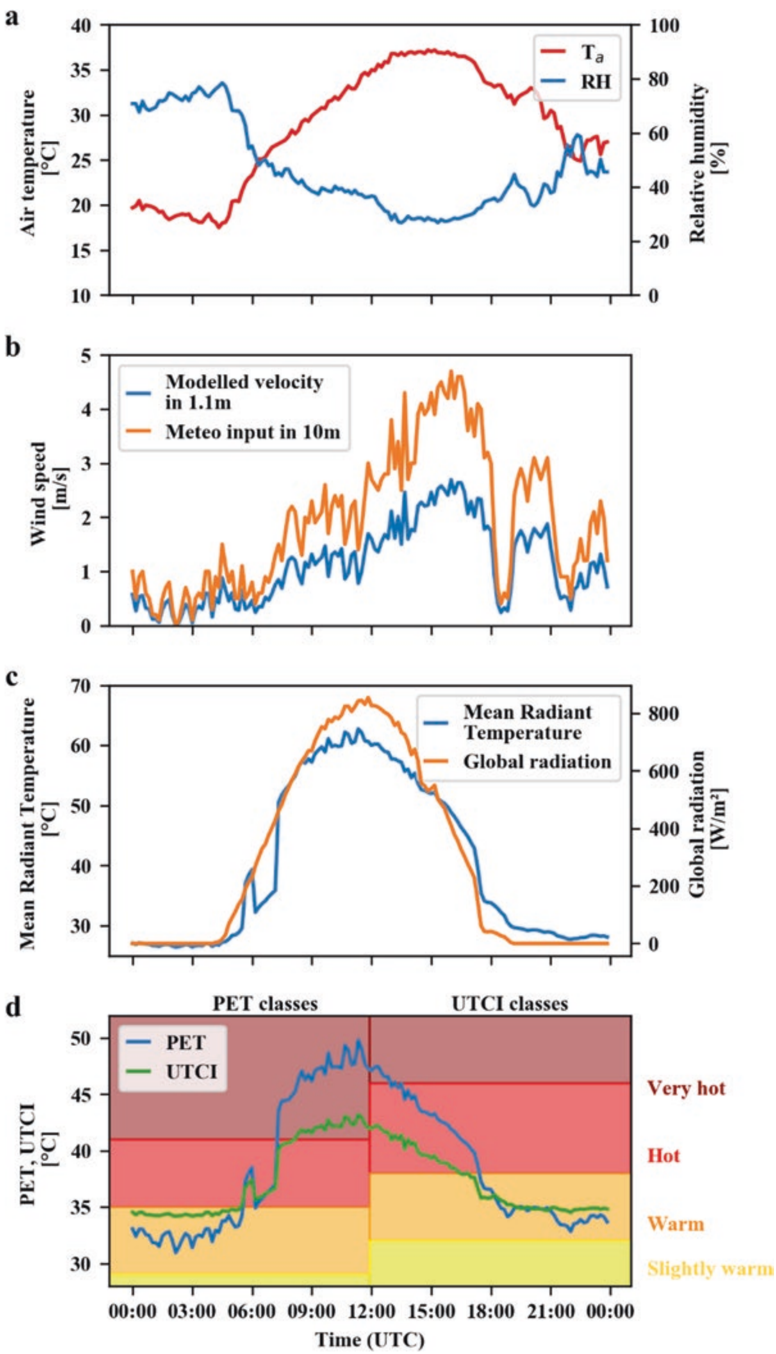


**Fig. 16.10** Time series representing the center of the study area. The dependency of the thermal indices (**d**) on air temperature (**a**), relative humidity (**a**), wind speed (**b**), and global radiation (**c**) as well as mean radiant temperature (**c**) is shown

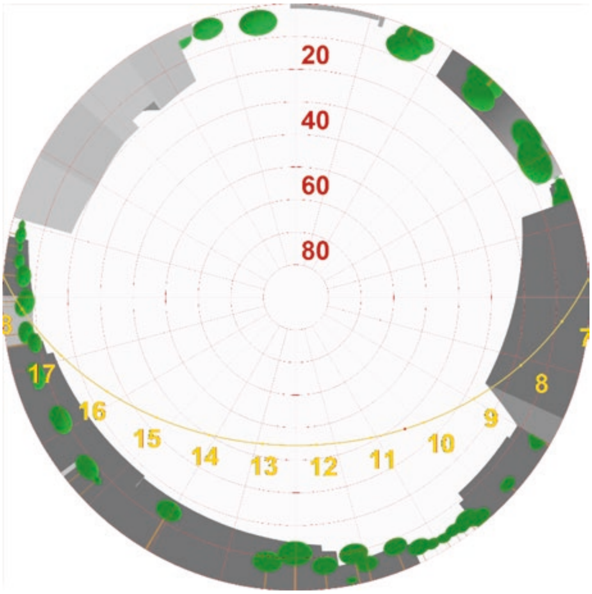


**Fig. 16.11** Fisheye image showing the urban morphology in the proximity and sun path (yellow) for the location of interest. The sun is hidden by buildings and vegetation in the morning and the evening

**Table 16.2** Classification of UTCI equivalent temperature in terms of thermal stress (Błażejczyk et al. 2013)

| UTCI (°C) | Level of physiological stress |
|---|---|
| ≥46 | Extreme heat stress |
| 38–46 | Very strong heat stress |
| 32–38 | Strong heat stress |
| 26–32 | Moderate heat stress |
| 9–26 | No thermal stress |
| 0–9 | Slight cold stress |
| −13 to 0 | Moderate cold stress |
| −27 to −13 | Strong cold stress |
| −40 to −27 | Very strong cold stress |
| <40 | Extreme cold stress |

appropriate for thermal assessment in human biometeorological studies in the outdoor area (Staiger et al. 2019). Based on these results, the former assumption of heat stress for given meteorological parameters is approved.

## 16.4 Conclusions

The time-independent RayMan and SkyHelios models are suitable models for human biometeorological analysis in urban areas. RayMan is advantageous over SkyHelios for selective point analysis, whereas the advanced SkyHelios model is much more applicable for the spatial estimation of the named, derived human biometeorological parameters: sky view factor, mean radiant temperature, and physiologically equivalent temperature. It is further applicable to compute radiational parameters: average short-wave albedo, long-wave emission coefficient, surface temperature, short- and long-wave radiation fluxes from the upper hemisphere and therefore global radiation, as well as sunshine duration, shading, and atmospheric parameters: wind speed and direction.

SkyHelios is superior to other methods to compute spatially resolved parameters of the radiation regime, e.g., sky view factor (Middel et al. 2018), due to fast spatial processing and selectable spatial resolution. This is achieved by utilization of fast-rendering 3D engines, instead of expensive ray-tracing approaches or manual field surveys. On the other hand, SkyHelios has some limitations due to missing spatially resolved scalar fields for air temperature and humidity. These parameters are assumed to be constant throughout the study area. Further, the calculations of wind speed and direction are not validated against measured data. Based on these results, SkyHelios and RayMan are appropriate tools to conduct urban microclimate simulations with the objective to analyze the urban bioclimate.

## References

American Society of Heating, Refrigerating and Air-Conditioning Engineers (2005). *2005 ASHRAE handbook: Fundamentals, inch-pound edition*. Norwood, MA: Books24x7.com. Retrieved September 19, 2019 from http://www.books24x7.com/marc.asp?bookid=18504

Błażejczyk, K., Jendritzky, G., Bröde, P., Fiala, D., Havenith, G., Epstein, Y., et al. (2013). An introduction to the Universal Thermal Climate Index (UTCI). *Geographia Polonica, 86*(1), 5–10. https://doi.org/10.7163/GPol.2013.1.

Bowler, D. E., Buyung-Ali, L., Knight, T. M., & Pullin, A. S. (2010). Urban greening to cool towns and cities: A systematic review of the empirical evidence. *Landscape and Urban Planning, 97*(3), 147–155. https://doi.org/10.1016/j.landurbplan.2010.05.006.

Bröde, P., Fiala, D., Błażejczyk, K., Holmér, I., Jendritzky, G., Kampmann, B., et al. (2012). Deriving the operational procedure for the Universal Thermal Climate Index (UTCI). *International Journal of Biometeorology, 56*(3), 481–494. https://doi.org/10.1007/s00484-011-0454-1.

Chen, Y.-C., & Matzarakis, A. (2018). Modified physiologically equivalent temperature—Basics and applications for western European climate. *Theoretical and Applied Climatology, 132*(3–4), 1275–1289. https://doi.org/10.1007/s00704-017-2158-x.

Fanger, P. O. (1972). *Thermal comfort: Analysis and applications in environmental engineering*. New York: McGraw-Hill.

Fiala, D., Havenith, G., Bröde, P., Kampmann, B., & Jendritzky, G. (2012). UTCI-Fiala multi-node model of human heat transfer and temperature regulation. *International Journal of Biometeorology, 56*(3), 429–441. https://doi.org/10.1007/s00484-011-0424-7.

Fröhlich, D. (2017). *Development of a microscale model for the thermal environment in complex areas*. Freiburg: Albert-Ludwigs-Universität Freiburg. https://doi.org/10.6094/UNIFR/11614.

Fröhlich, D., & Matzarakis, A. (2013). Modeling of changes in thermal bioclimate: Examples based on urban spaces in Freiburg, Germany. *Theoretical and Applied Climatology, 111*(3–4), 547–558. https://doi.org/10.1007/s00704-012-0678-y.

Fröhlich, D., & Matzarakis, A. (2016). A quantitative sensitivity analysis on the behaviour of common thermal indices under hot and windy conditions in Doha, Qatar. *Theoretical and Applied Climatology, 124*(1–2), 179–187. https://doi.org/10.1007/s00704-015-1410-5.

Fröhlich, D., & Matzarakis, A. (2018). Spatial estimation of thermal indices in urban areas—Basics of the SkyHelios model. *Atmosphere, 9*(6), 209. https://doi.org/10.3390/atmos9060209.

Fröhlich, D., Gangwisch, M., & Matzarakis, A. (2019). Effect of radiation and wind on thermal comfort in urban environments—Application of the RayMan and SkyHelios model. *Urban Climate, 27*, 1–7. https://doi.org/10.1016/j.uclim.2018.10.006.

Gagge, A. P., Fobelets, A. P., & Berglund, L. G. (1986). A standard predictive index of human response to the thermal environment. *ASHRAE Transactions (United States), 92*, 2B.

GDAL/OGR Contributors. (2019). *GDAL/OGR geospatial data abstraction software library*. Retrieved March 15, 2019 from http://gdal.org

Gonzalez, R. R., Nishi, Y., & Gagge, A. P. (1974). Experimental evaluation of standard effective temperature a new biometeorological index of man's thermal discomfort. *International Journal of Biometeorology, 18*(1), 1–15. https://doi.org/10.1007/BF01450660.

Gröger, G., Kolbe, T. H., Nagel, C., & Häfele, K.-H. (2012). In G. Gröger, T. H. Kolbe, C. Nagel, & K.-H. Häfele (Eds.), *OGC city geography markup language (CityGML) encoding standard*. Wayland, MA: 2.0.0. Open Geospatial Consortium.

Hämmerle, M., Gál, T., Unger, J., & Matzarakis, A. (2011). Comparison of models calculating the sky view factor used for urban climate investigations. *Theoretical and Applied Climatology, 105*(3–4), 521–527. https://doi.org/10.1007/s00704-011-0402-3.

Havenith, G., Fiala, D., Błażejczyk, K., Richards, M., Bröde, P., Holmér, I., et al. (2012). The UTCI-clothing model. *International Journal of Biometeorology, 56*(3), 461–470. https://doi.org/10.1007/s00484-011-0451-4.

Herrmann, J., & Matzarakis, A. (2012). Mean radiant temperature in idealised urban canyons—Examples from Freiburg, Germany. *International Journal of Biometeorology, 56*(1), 199–203. https://doi.org/10.1007/s00484-010-0394-1.

Höppe, P. (1984). *Die Energiebilanz des Menschen* (Vol. 49). München: Universität München, Meteorologisches Institut.

Höppe, P. (1993). Heat balance modelling. *Experientia, 49*(9), 741–746. https://doi.org/10.1007/BF01923542.

Höppe, P. (1999). The physiological equivalent temperature—A universal index for the biometeorological assessment of the thermal environment. *International Journal of Biometeorology, 43*(2), 71–75. https://doi.org/10.1007/s004840050118.

Hwang, R.-L., Lin, T.-P., & Matzarakis, A. (2011). Seasonal effects of urban street shading on long-term outdoor thermal comfort. *Building and Environment, 46*(4), 863–870. https://doi.org/10.1016/j.buildenv.2010.10.017.

Jendritzky, G. (1990). *Methodik zur räumlichen Bewertung der thermischen Komponente im Bioklima des Menschen: fortgeschriebenes Klima-Michel-Modell*. Hannover: Akademie für Raumforschung und Landesplanung.

Jendritzky, G., de Dear, R., & Havenith, G. (2012). UTCI—Why another thermal index? *International Journal of Biometeorology, 56*(3), 421–428. https://doi.org/10.1007/s00484-011-0513-7.

Kasten, F. (1980). A simple parameterization of the pyrheliometric formula for determining the Linke turbidity factor. *Meteorologische Rundschau, 33*, 124–127.

Kasten, F., & Young, A. T. (1989). Revised optical air mass tables and approximation formula. *Applied Optics, 28*(22), 4735.

Ketterer, C., & Matzarakis, A. (2014). Human-biometeorological assessment of heat stress reduction by replanning measures in Stuttgart, Germany. *Landscape and Urban Planning, 122*, 78–88. https://doi.org/10.1016/j.landurbplan.2013.11.003.

Ketterer, C., Gangwisch, M., Fröhlich, D., & Matzarakis, A. (2017). Comparison of selected approaches for urban roughness determination based on Voronoi cells. *International Journal of Biometeorology, 61*(1), 189–198. https://doi.org/10.1007/s00484-016-1203-2.

Matzarakis, A., & Matuschek, O. (2011). Sky view factor as a parameter in applied climatology rapid estimation by the SkyHelios model. *Meteorologische Zeitschrift, 20*, 39–45. https://doi.org/10.1127/0941-2948/2011/0499.

Matzarakis, A., & Mayer, H. (1996). Another kind of environmental stress: Thermal stress. *WHO Newsletter, 18*, 7–10.

Matzarakis, A., Mayer, H., & Iziomon, M. G. (1999). Applications of a universal thermal index: Physiological equivalent temperature. *International Journal of Biometeorology, 43*(2), 76–84. https://doi.org/10.1007/s004840050119.

Matzarakis, A., Rutz, F., & Mayer, H. (2007). Modelling radiation fluxes in simple and complex environments—Application of the RayMan model. *International Journal of Biometeorology, 51*(4), 323–334. https://doi.org/10.1007/s00484-006-0061-8.

Matzarakis, A., Rutz, F., & Mayer, H. (2010). Modelling radiation fluxes in simple and complex environments: Basics of the RayMan model. *International Journal of Biometeorology, 54*(2), 131–139. https://doi.org/10.1007/s00484-009-0261-0.

Matzarakis, A., Fröhlich, D., Ketterer, C., & Martinelli, L. (2018). Urban bioclimate and micro climate: How to construct cities in the era of climate change. In *Climate change and sustainable heritage* (pp. 38–61). Newcastle upon Tyne: Cambridge Scholars Publishing.

Mayer, H., & Höppe, P. (1987). Thermal comfort of man in different urban environments. *Theoretical and Applied Climatology, 38*(1), 43–49. https://doi.org/10.1007/BF00866252.

Middel, A., Lukasczyk, J., Maciejewski, R., Demuzere, M., & Roth, M. (2018). Sky view factor footprints for urban climate modeling. *Urban Climate, 25*, 120–134. https://doi.org/10.1016/j.uclim.2018.05.004.

Middel, A., Lukasczyk, J., Zakrzewski, S., Arnold, M., & Maciejewski, R. (2019). Urban form and composition of street canyons: A human-centric big data and deep learning approach. *Landscape and Urban Planning, 183*, 122–132. https://doi.org/10.1016/j.landurbplan.2018.12.001.

Mirzaei, P. A., & Haghighat, F. (2010). Approaches to study urban heat island—Abilities and limitations. *Building and Environment, 45*(10), 2192–2201. https://doi.org/10.1016/j.buildenv.2010.04.001.

Ogre Development Team. (2019). *OGRE—Open source 3D graphics engine*. Retrieved March 15, 2019 from https://www.ogre3d.org/

Oke, T. R. (1987). *Boundary layer climates* (2 new ed.). London: Routledge.

Open Source Geospatial Foundation. (2018). *QGIS geographic information system*. Retrieved from http://qgis.osgeo.org

Staiger, H., Laschewski, G., & Grätz, A. (2012). The perceived temperature—A versatile index for the assessment of the human thermal environment. Part A: Scientific basics. *International Journal of Biometeorology, 56*(1), 165–176. https://doi.org/10.1007/s00484-011-0409-6.

Staiger, H., Laschewski, G., & Matzarakis, A. (2018). A short note on the inclusion of sultriness issues in perceived temperature in mild climates. *Theoretical and Applied Climatology, 131*(1–2), 819–826. https://doi.org/10.1007/s00704-016-2013-5.

Staiger, H., Laschewski, G., & Matzarakis, A. (2019). Selection of appropriate thermal indices for applications in human biometeorological studies. *Atmosphere, 10*(1), 18. https://doi.org/10.3390/atmos10010018.

Valko, P. (1966). Die Himmelsstrahlung in ihrer Beziehung zu verschiedenen Parametern. *Archiv für Meteorologie, Geophysik und Bioklimatologie, Serie B, 14*(3–4), 336–359.

VDI. (1988). *Stadtklima und Luftreinhaltung*. Berlin: Springer. https://doi.org/10.1007/978-3-662-10001-1.

VDI. (1994). *3789 Part 2: Environmental meteorology. Interactions between atmosphere and surfaces, calculation of short-wave and long-wave radiation* (p. 52). Düsseldorf: VDI.

VDI. (2008). *VDI 3787, Part 2: Environmental meteorology, Methods for the human biometeorological evaluation of climate and air quality for urban and regional planning at regional level*.

Zardo, L., Geneletti, D., Pérez-Soba, M., & Van Eupen, M. (2017). Estimating the cooling capacity of green infrastructures to support urban planning. *Ecosystem Services, 26*, 225–235. https://doi.org/10.1016/j.ecoser.2017.06.016.